AIAA JOURNAL
Vol. 46, No. 9, September 2008

Aeroelastic Solutions Using the Nonlinear Frequency-Domain Method

Farid Kachra* and Siva K. Nadarajah†
McGill University, Montreal, Quebec H3A 2S6, Canada

DOI: 10.2514/1.27602

In this work, both fully implicit time-domain and nonlinear frequency-domain methods are used to compute aeroelastic solutions in transonic flows. Specifically, flutter boundaries for a two-dimensional NACA64A010 airfoil are calculated and compared with preexisting numerical results. The second-order backward-difference time-accurate scheme will serve as our numerical benchmark when determining the computational efficiency of the nonlinear frequency-domain method. Comparable results between the time-domain and nonlinear frequency-domain approaches will further justify the nonlinear frequency-domain method as an efficient alternative to the study of unsteady periodic problems. A temporal resolution study will establish the required number of modes or time steps per period required for unsteady transonic flows.

Nomenclature

b	=	boundary velocity component
D	=	artificial dissipation flux
E	=	internal energy
F	=	numerical flux vector
f	=	flux vector
h	=	plunging coordinate
i, j	=	cell indices
k	=	wave number
M	=	Mach number
n	=	time indices
p	=	pressure
R	=	residual
$\hat{R}$	=	Fourier coefficient of residual
S	=	face areas of computational cell
t	=	time
t^*	=	pseudotime
u	=	velocity (physical domain)
V	=	cell volume
w	=	state vector
$\hat{w}$	=	Fourier coefficient of state vector
x	=	coordinates (physical domain)
α	=	angle of attack
ϵ	=	adjustable constant for artificial dissipation scheme
ξ	=	coordinates (computational domain)
ρ	=	density
ω_r	=	reduced frequency

I. Introduction

HARDWARE limitations restrict the level of problem complexity one can pursue, but a more important limitation is the execution efficiency of the algorithm used. The ability to accurately model the time evolution of the flow can be computationally demanding, especially when dealing with 3-D problems. It has been estimated[‡] that the computational cost of a typical multistage compressor and turbine calculation using parallel processing of 750 processors working 8 h a day would take over 1300 days (estimates are based on the flow through a 23-blade row compressor). Even though most of the computational time in periodic problems is spent in resolving the decay of the initial transients, users are typically only concerned with the data after a periodic steady state has been reached. As a result, there has been much effort focused on the development of efficient and practical alternatives to the study of unsteady periodic problems.

Examples of engineering applications in which the flow is unsteady yet periodic include flows resulting from helicopter rotor motion, turbomachinery blades, and aerodynamic flutter. Linearized frequency-domain and deterministic stress methods [1] are examples of periodic methods that are widely used in industry. Unfortunately, the inability of these methods to accurately model the solution becomes evident for systems that contain strong nonlinearities. The harmonic balance technique, a pseudospectral approach initially proposed by Hall et al. [2] and later modified by McMullen [3], has been validated against both the Euler and Navier–Stokes equations for a number of unsteady periodic problems. The cost associated with spectral methods such as McMullen's nonlinear frequency-domain method (NLFD) is proportional to the cost of the steady-state solution multiplied by the number of desired temporal modes. For inviscid flow, it has been shown by McMullen that to accurately model an oscillating airfoil pitching about its quarter-chord, a temporal resolution of only one mode above the fundamental frequency (or, equivalently, three time samples per period) is needed using the NLFD method versus the 36 time samples needed with a backward-difference formulation of the time derivative [4]. The ability of the NLFD method to account for strong nonlinearities and converge to the exact solution exponentially is the reason why it is used in this work to solve for the transonic flutter boundary of a NACA64A010 airfoil.

The transonic dip, a phenomena extensively studied by Mykytow [5], showed a significant decrease in the flutter speed of a swept-wing subject to transonic flight conditions, and according to Ashley [6], it is the phase lag of the shock wave motion that prompts a large out-of-phase force that precipitates the phenomena. Through experimental work, Farmer and Hanson [7] later showed the importance of airfoil thickness on the unsteady characteristics of the aerodynamics loads. Bendiksen and Kousen [8] employed an explicit flow solver coupled with a structural integrator based on the convolution integral and performed a transonic flutter analysis using the Euler equations. A demonstration of three-dimensional aeroelastic solutions for swept wings was presented by Guruswamy [9,10]. Robinson et al. [11]

Presented as Paper 2980 at the 25th Applied Aerodynamics Conference, San Francisco, 5–8 June 2006; received 2 October 2006; revision received 9 November 2007; accepted for publication 6 April 2008.

*Graduate Student, Department of Mechanical Engineering, Computational Fluid Dynamics Laboratory, 688 Sherbrooke Street West, Room 719. Student Member AIAA.

†Assistant Professor, Department of Mechanical Engineering, Computational Fluid Dynamics Laboratory, 688 Sherbrooke Street West, Room 711.

‡Personal communication with R. Davis, Jan.–Dec. 2001.

incorporated a mesh-deformation algorithm to acquire time-marching flutter calculations for a 45-deg swept-back wing using an Euler code. Flutter characteristics of wing 445.6 were attempted by Rausch et al. [12] with an unstructured Euler solver. Alonso and Jameson [4] ensured simultaneous convergence of both fluid flow and structural models using a fully implicitly driven multigrid strategy. Willcox and Peraire [13] proposed coupling an lower/upper factorization scheme with the generalized minimal residual algorithm to acquire convergence of both the flowfield and structural equations of motion at each time step. High-fidelity aeroelastic solutions for complex three-dimensional geometries have been extensively studied by many researchers [14–17]. A comprehensive overview of modern developments for computational aeroelasticity is provided by Bendiksen [18], Schuster et al. [19], and Bennett and Edwards [20].

The main objective of this work is to further extend the NLFD method as an efficient and accurate alternative for computing aeroelastic solutions in the transonic regime. The approach will be used to compute flutter boundaries at different speed indices V_f in the transonic regime using the Isogai [21] swept-wing model structural parameters. Time-accurate solutions by Alonso and Jameson [4] and Willcox and Peraire [13] will serve as our numerical benchmark when determining the overall computational savings one can achieve by using the NLFD method.

II. Euler Equations

A. Governing Equations in Semidiscrete Form

The Cartesian coordinates and velocity components are denoted by x_1, x_2, and u_1, u_2. Einstein notation simplifies the presentation of the equations, in which summation over $i = 1$ to 2 is implied by a repeated index i. The two-dimensional Euler equations then take the form

$$\frac{\partial w}{\partial t} + \frac{\partial f_i}{\partial x_i} = 0 \quad \text{in } \mathcal{D} \tag{1}$$

where the state vector w and inviscid flux vector f are described, respectively, by

$$w = \begin{Bmatrix} \rho \\ \rho u_1 \\ \rho u_2 \\ \rho E \end{Bmatrix}, \qquad f_i = \begin{Bmatrix} \rho(u_i - b_i) \\ \rho u_1(u_i - b_i) + p\delta_{i1} \\ \rho u_2(u_i - b_i) + p\delta_{i2} \\ \rho E(u_i - b_i) + pu_i \end{Bmatrix} \tag{2}$$

where ρ is the density, b_i is the boundary Cartesian velocity component, E is the total energy, and δ_{ij} is the Kronecker delta function. The pressure is determined by the equation of state

$$p = (\gamma - 1)\rho\left\{E - \tfrac{1}{2}(u_i u_i)\right\}$$

The simulations contained in this research are restricted to rigid-mesh translation and rotation. As a result, we can write Eq. (1) as the product of the cell volume and temporal derivative of the state vector w at the cell center. In terms of cell volumes and the local residual $R(w)$ (composed of both convective and dissipative fluxes), Eq. (1) can be written in semidiscrete form as

$$V\frac{\mathrm{d}w}{\mathrm{d}t} + R(w) = 0 \quad \text{in } \mathcal{D} \tag{3}$$

where the residual $R(w)$ can then be written in computational space as

$$R(w) = \frac{\partial F_i}{\partial \xi_i} \tag{4}$$

where the inviscid flux contributions are now defined with respect to the computational cell faces by $F_i = S_{ij} f_j$, and the quantity $S_{ij} = JK_{ij}^{-1}$ represents the projection of the ξ_i cell face along the x_j axis, where $K_{ij} = (\partial x_i/\partial \xi_j)$ and $J = \det(K)$.

The approximation of the flux vector F that ensures numerical stability is the subject of shock-capturing theory. The convective component of the flux is evaluated at the face of the control volume using averages of the flux vector evaluated at the cell centers adjacent to the face. The dissipative component of the flux is a blended mix of first- and third-order fluxes first introduced by Jameson et al. [22]. To accelerate the convergence the code employs local time-stepping, implicit residual smoothing, and a 5-W-level multigrid strategy. At the far-field boundary, a characteristic-based boundary condition using Riemann invariants is imposed. The method extrapolates the outward waves based on interior information and calculates incoming waves using the freestream conditions.

B. Time-Accurate Method

Applying the set of Eqs. (3) in terms of each cell in our mesh results in

$$\frac{\mathrm{d}}{\mathrm{d}t}(w_{i,j}^{n+1} V_{i,j}) + R(w_{i,j}^{n+1}) = 0 \tag{5}$$

where $V_{i,j}$ is the volume of the i,j cell and $R(w_{i,j})$ is the residual term introduced by the discretization of Eq. (1). The time-derivative term can be approximated by a kth-order implicit backward-difference formula. A second-order discretization provides for an A-stable method, as demonstrated by Jeltsch [23] on a linear differential equation. Gear [24] showed that the third-order backward-difference formula is stiffly stable, and Melson et al. [25] demonstrated that the fourth-order scheme is conditionally stable. In the present work, due to the robustness of the scheme, the second-order backward-difference formula will be used to discretize the time derivative.

Next, we can define a modified residual $R^*(w_{i,j})$ as

$$R^* = \frac{V_{i,j}}{\mathrm{d}t}\left[\frac{3}{2}w_{i,j}^{n+1} - 2w_{i,j}^{n} + \frac{1}{2}w_{i,j}^{n-1}\right] + R(w_{i,j}^{n+1}) \tag{6}$$

Making use of a five-stage Runge–Kutta scheme, we are able to minimize the modified residual via a steady-state march in pseudotime t^*:

$$\frac{\mathrm{d}}{\mathrm{d}t^*}(w_{i,j}^{n+1}) + R^*(w_{i,j}^{n+1}) = 0 \tag{7}$$

Because of the highly nonlinear nature of the governing equations, convergence acceleration techniques such as residual averaging, implicit time-stepping, and multigrid strategies are used.

C. Nonlinear Frequency-Domain Method

The derivation of the NLFD method starts with Eq. (3) and assumes that the vector of flow variables w and local residual R can be represented by separate Fourier series:

$$w = \sum_{k=-\frac{N}{2}}^{\frac{N}{2}-1} \hat{w}_k e^{ikt}, \qquad R = \sum_{k=-\frac{N}{2}}^{\frac{N}{2}-1} \hat{R}_k e^{ikt} \tag{8}$$

where $i = \sqrt{-1}$. The Fourier representations are then substituted into the semidiscrete form of the governing equations, as described in Eq. (3), to yield

$$V\frac{d}{dt}\left[\sum_{k=-\frac{N}{2}}^{\frac{N}{2}-1} \hat{w}_k e^{ikt}\right] + \sum_{k=-\frac{N}{2}}^{\frac{N}{2}-1} \hat{R}_k e^{ikt} = 0 \quad \text{in } \mathcal{D} \tag{9}$$

As a result,

$$\hat{R}_k^* = ikV\hat{w}_k + \hat{R}_k \tag{10}$$

forms the new unsteady residual in the frequency domain for each wave number and must be solved iteratively. The solver attempts to find a solution w that drives this system of equations to zero for all wave numbers. However, just like the modified residual (6) in the time-accurate case, the unsteady residual processed at any given

iteration R^* will be finite. The nonlinearity of the unsteady residual, and hence the bulk of our computing effort, stems from the spatial operator R. There are two approaches to calculating the spatial operator expressed in the frequency domain. The first uses a complex series of convolution sums to calculate $\hat{R}_k$ directly from $\hat{w}_k$. This approach is discarded due to its massive complexity (considering artificial dissipation schemes and turbulence modeling) and cost that scales quadratically with the number of modes N. This paper implements a pseudospectral approach that relies on the computational efficiency of the fast Fourier transform (FFT). To calculate R in the frequency domain, several transformations between the physical and frequency domains are performed by FFT. The computational cost of this transform scales like $N\log(N)$, a significant savings over a similar method that uses convolution sums and scales like N^2. A diagram detailing the transformations used by the pseudospectral approach at each stage of the modified multistage Runge–Kutta scheme is provided in Fig. 1.

The pseudospectral approach begins by initializing the state vector $w(t)$ at all time instances. At the first iteration, $w(t)$ will take on the value of the initial condition, and for subsequent iterations, the values are based on the previous iterations. At each of these time instances, the steady-state operator $R(w(t))$ can be computed by summing the convective and artificial dissipation fluxes, as mentioned in the previous subsection. A FFT is then used to transform the state vector and spatial operator to the frequency domain in which $\hat{w}_k$ and $\hat{R}_k$ are known for all wave numbers. The unsteady residual $\hat{R}_k^*$ can then be calculated by adding $\hat{R}_k$ to the spectral representation of the temporal derivative $ikV\hat{w}_k$. The iteration is advanced and the $\hat{w}_k$ is updated. Using an inverse FFT, $\hat{w}_k$ is then transformed back to the physical space, resulting in a state vector $w(t)$ sampled at evenly distributed intervals over the time period. The wall and far-field boundary conditions are imposed within the time domain. Consistent with the time-accurate approach, we can numerically integrate our residual in fictitious time t^*, resulting in the following equation:

$$V\frac{\mathrm{d}\hat{w}_k}{\mathrm{d}t^*} + \hat{R}_k^* = 0 \tag{11}$$

In the NLFD case, an unsteady residual exists for each wave number used in the solution and the pseudotime derivative acts as a gradient to drive the absolute value of all of these components to convergence simultaneously. In synopsis, the NLFD approach can be implemented into any existing time-accurate flow solver with the following two primary modifications. First, the state vector must be modified to allow an additional dimension to hold the value at various time steps. This is unlike the time-accurate approach, in which the second-order backward-difference approach only required the state vector to be stored at three time levels. For the NLFD approach, if three or more time steps are employed, the memory cost increases. Second, calls to FFT routines must be implemented within the time-stepping scheme to perform both the FFT and inverse FFT.

An important limitation of the current implementation is the assumption that the cell volume V is constant in time. In the work presented in this paper, a rigid-body translation and rotation is employed and this assumption is therefore valid. The volume $V(t)$, an extension of the method for unsteady motions in which small grid deformations are present, will be a function of time and must be included in Eq. (9) within the time derivative. However, for cases in which large grid deformations are observed that might include grid adaptation that could potentially increase or decrease the number of cells to improve the quality of the grid for the flow solver, an interpolation of the state vector $w(t)$ to a common fixed point in space might be needed to transform the state vector to the frequency domain. Nevertheless, such an approach would reduce the order of the method and cast the approach as a reduced-order model.

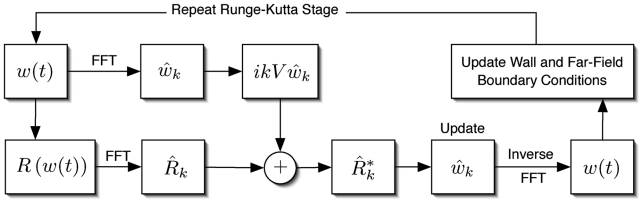

Fig. 1 Simplified data-flow diagram of the time advancement scheme illustrating the pseudospectral approach used in calculating the nonlinear spatial operator *R*.

III. Aeroelastic Model

The section-wing model to be used in this work (see Fig. 2) is a 2-D airfoil with plunging and pitching degrees of freedom. The governing coupled second-order structural equations of motion can be written as

$$m\ddot{h} + S_\alpha\ddot{\alpha} + K_h h = -L, \qquad S_\alpha\ddot{h} + I_\alpha\ddot{\alpha} + K_\alpha\alpha = M_{ea}$$

or, in matrix form,

$$[M]\{\ddot{q}\} + [K]\{q\} = [F]$$

where

$$[M] = \begin{Bmatrix} m & S_\alpha \\ S_\alpha & I_\alpha \end{Bmatrix}, \quad [K] = \begin{Bmatrix} K_h & 0 \\ 0 & K_\alpha \end{Bmatrix}, \quad [F] = \begin{Bmatrix} -L \\ M_{ea} \end{Bmatrix}, \quad [q] = \begin{Bmatrix} h \\ \alpha \end{Bmatrix} \tag{12}$$

L is the lift (positive up); M_{ea} is the moment about the elastic axis (positive nose up); S_α, I_α, K_h, and K_α are the static imbalance, moment of inertia, bending stiffness and torsional stiffness, respectively; h is the plunging coordinate (positive down); and α is the angle of attack (clockwise positive).

A. Discretization Using the Central-Backward-Difference Formula

The time-accurate steady-state solution to the fluid–structure problem considered herein is dependent on the exchange of four variables: h, α, L, and M_{ea}. For a given time step n, N multigrid cycles are performed to calculate L and M_{ea}, where N is the required number of multigrid cycles to ensure a sufficient reduction in the residual. Control is then transferred to the structural solver so that the structural equations can be solved for h and α. Given the new plunge and pitch, a new position for the airfoil can be determined. After passing this information to the flow solver, a new L and M_{ea} can be computed. This process repeats several times, depending on the number of multigrid cycles employs at each real time step. In general, exchange of loads and displacements occurred every $N = 2$ multigrid cycles. This constitutes a tight coupling procedure, as suggested by Alonso and Jameson [4] and ensures a simultaneous convergence of both the governing aerodynamic and structural equations.

The structural integrator used in this work takes a form similar to that of the classical beta Newmark scheme. Discretizing the structural equations of motion using a central finite difference representation of the first and second derivatives, we can write

$$[A]_1\{q\}_{n+1} = [A]_2 + [A]_3\{q\}_n + [A]_4\{q\}_{n-1}$$

where

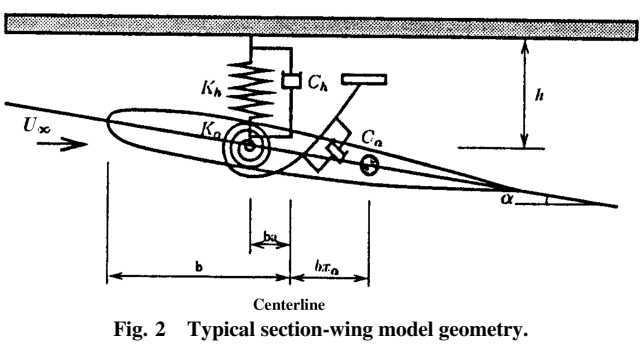

Fig. 2 Typical section-wing model geometry.

$$[A]_1 = \left[\frac{M}{\Delta t^2} + \frac{K}{3}\right], \qquad [A]_2 = \frac{1}{3}[F_{n+1} + F_n + F_{n-1}],$$
$$[A]_3 = \left[\frac{2M}{\Delta t^2} - \frac{K}{3}\right], \qquad [A]_4 = \left[-\frac{M}{\Delta t^2} - \frac{K}{3}\right]$$

The plunge and pitch at time step $n+1$ can now be solved by a simple matrix inversion.

B. Spectral Method Representation

Given the periodic nature of the problem, both the plunging displacement h and angle of attack α can be written in spectral form as

$$h = \sum_{k=-\frac{N}{2}}^{\frac{N}{2}-1} \hat{h}_k e^{ikt}, \qquad \alpha = \sum_{k=-\frac{N}{2}}^{\frac{N}{2}-1} \hat{\alpha}_k e^{ikt} \tag{13}$$

Taking advantage of the orthogonality of the Fourier terms and substituting Eqs. (13) into our structural equations yields a separate equation for each wave number k in the solution

$$(K_h - mk^2)\hat{h}_k - (S_\alpha k^2)\hat{\alpha}_k = -\hat{L}_k,$$
$$-(S_\alpha k^2)\hat{h}_k + (K_\alpha - I_\alpha k^2)\hat{\alpha}_k = \hat{M}_{ea_k}$$

After solving the preceding simple system for $\hat{h}_k$ and $\hat{\alpha}_k$ for each wave number, we can use an inverse FFT to determine our displacements at k equally spaced points in our period. The displacement velocities $\dot{h}$ and $\dot{\alpha}$ are computed using a trigonometric interpolation of the displacements followed by a backward difference of adjacent points.

Unlike the time-accurate solver, in which the solution is marched forward in time, the NLFD solver computes the flow solution at all time steps simultaneously at each multigrid cycle or pseudotime step. To fully converge both the NLFD flow solver and the structural solver to a periodic steady-state solution, exchange of information between the two codes occurs every N multigrid cycles. In general, N was set to 15 cycles because this provided a three- to four-order reduction in the residual. This operation was designated as one period and the process continues until a fully converged solution is established. However, in the case of the time-accurate procedure, as mentioned in the previous subsection, transfer of information occurred at every two multigrid cycles. This was possible because the flow solution at the previous time step, $n-1$, was fully established and frequent exchange of information to preserve a tight coupling between the two solvers was feasible. However, in the case of the NLFD solver, it takes several iterations before the flow solution is well defined; hence, transfer of information can only take place at these junctures to guarantee a tight coupling.

IV. Results

The results presented herein are based on two separate flow solvers. UTSYN103, a time-accurate code used to solve the unsteady Euler and Navier–Stokes equations, was originally developed by Nadarajah and Jameson [26] and Nadarajah et al. [27]. UFSYN103, a slightly modified pseudospectral representation of UTSYN103, was developed by Nadarajah et al. [27]. The aeroelastic solutions presented in this work are based on the Isogai [21] case A for a two-dimensional swept-wing model using a NACA64A010 airfoil. Structural constants are $x_\alpha = 1.8$, $r_\alpha^2 = 3.48$, $a = -2.0$, $w_h = 100$ rad/s, $w_\alpha = 100$ rad/s, and $\mu = 60$. The reduced frequency and speed index are defined as $k_c = \omega c/2V_\infty$ and $V_f = V_\infty/bw_\alpha\sqrt{\mu}$, respectively. Note that a is the location of the pivot point and is proportional to the half-chord length. The pivot point is located one chord length forward of the airfoil midchord position and is chosen to simulate the aeroelastic response of a swept-back wing.

The base time-accurate and NLFD solvers have been validated for both two- and three-dimensional flows by Nadarajah and Jameson [28,29]. Before proceeding to the aeroelastic simulations, a brief discussion of the computational cost of the two codes is presented in the next few paragraphs, because this will provide for a basis of comparison between the two approaches.

All numerical simulations were performed using a structured 193×33 mesh of a NACA64A010 airfoil section, as illustrated in Fig. 3. The code convergence for both the time-accurate and NLFD solvers are presented in Fig. 4 for a flutter case at Mach 0.85. The procedure employed to obtain aeroelastic solutions will be provided in detail in Sec. IV.B. Here, we will only discuss the convergence properties of each code. The time-accurate code reaches machine-zero accuracy within 150 multigrid cycles. The convergence plot for the time-accurate run shown in Fig. 4 depicts the convergence at a specific time step. All other time steps have approximately similar convergence rates. The NLFD code reaches machine-zero accuracy between 500 and 600 cycles, depending on the number of modes. There are three important observations. First, the convergence rate of the NLFD solver is independent of the number of harmonics. For the three-time-step case, both modes, the zeroth (represented as NLFD-3 0 mode) and the first mode, converge at the same rate. The same is true for the five- and seven-time-step cases, albeit at a slightly slower convergence rate.

Second, both codes exhibit a similar convergence rate for the first 15 to 25 multigrid cycles. The residuals reach to a level between 1E-3 and 1E-4, which is sufficient for engineering accuracy. Above 30 multigrid cycles, the convergence rate of the NLFD solver reduces for all cases. Therefore, the aeroelastic solutions that will be presented use just 15 multigrid cycles per time step for the time-accurate cases and 15 cycles per period for the NLFD cases.

Finally, the CPU time for the NLFD solver is higher per multigrid cycle than with the time-accurate code. For the NLFD method, if three time steps are employed to resolve the solution, then all three

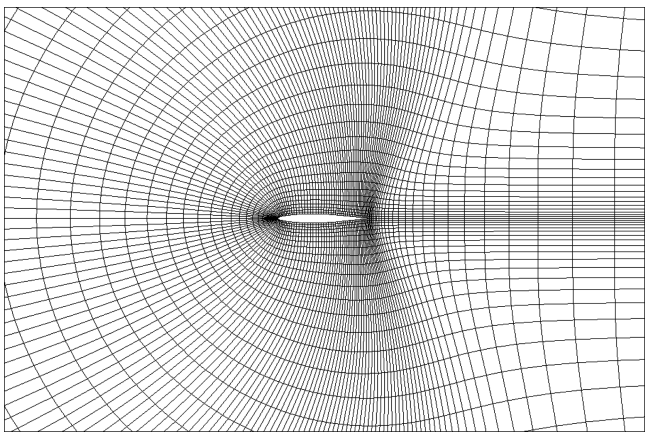

Fig. 3 NACA64A010 193 × 33 C-mesh.

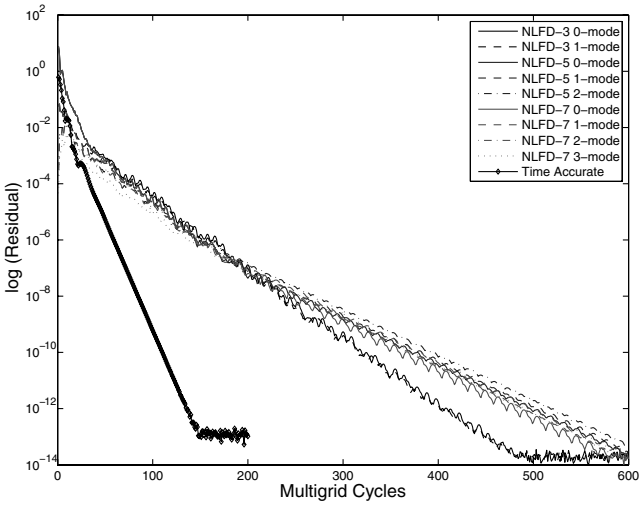

Fig. 4 Convergence of time-accurate and NLFD solvers at $M_\infty = 0.85$ and $V_f = 0.533$.

time steps are advanced at each multigrid cycle. Thus, the computational cost per multigrid cycle is directly proportional to the number of time steps used to represent the solution. However, the computational cost per multigrid cycle is higher for the NLFD solver, due to the cost associated with using the FFT. At each multigrid cycle, a forward and backward transform is performed at each stage of the five-stage Runge–Kutta scheme. This additional cost amounts to approximately 2% for a three-time-step case and 2.6% for five time steps, as reported by McMullen [3] and Nadarajah et al. [27].

A. Temporal Resolution

In this subsection, we discuss the required number of time steps needed to obtain a converged flutter solution with respect to temporal accuracy for both the time-accurate and NLFD approaches. The computational cost for the various factors established in the previous subsection will be used to provide a proper benchmark between the two codes. Figures 5 and 6 illustrate a comparison of the plunge and angle-of-attack displacements for a neutral response at a freestream Mach number of 0.85 and speed index $V_f = 0.533$. Time-accurate solutions with 18, 24, 36, and 72 time steps per period are compared against a NLFD solution with one harmonic, which uses three time steps per period. Both the 18- and 24-time-step cases exhibit visual differences for the displacement and phase against the 36- and 72-time-step solutions. The 72-time-step case serves as a benchmark and the 36-time-step-per-period solution provides for an approximate minimum number of time steps to demonstrate a converged aeroelastic solution. The one harmonic NLFD case compares very well against the 36- and 72-time-step cases.

A quantitative comparison between the various time-accurate and NLFD solutions are tabulated in Table 1. A comparison among the time-accurate solutions demonstrate that at least 36 time steps per period are required to acquire plunge and pitch values accurate up to three decimal places. However, even though the 18- and 24-time-step-per-period cases provided less than satisfactory displacements, the flutter frequency is comparable with that produced by larger-number time-step cases. A comparison between the NLFD solution and the time-accurate results provides clear evidence that one mode is sufficient to acquire plunge and pitch displacements equivalent to the 36-time-step solution. A further inquiry into the differences among the various solutions are provided in Table 2. Here, the l_2-norm of the plunge and pitch displacement errors are provided. The 72-time-step-per-period case is used as the base solution. The table shows that the one harmonic solution provides for a level of accuracy similar to, if not slightly better than, the 36-time-step-per-period case. This reinforces the observation that the NLFD approach with just one mode provides for accurate aeroelastic solutions.

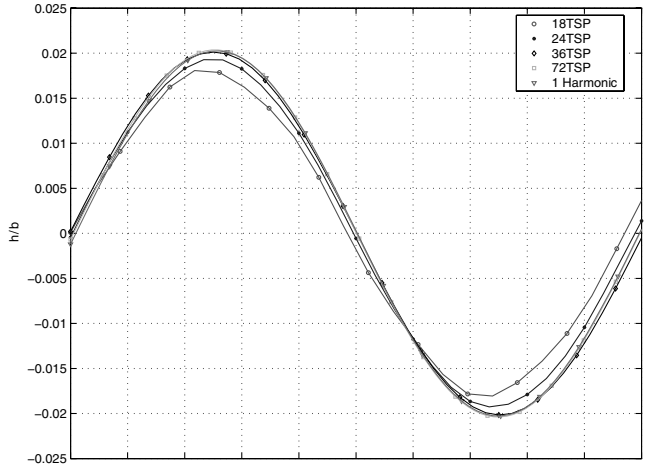

Fig. 5 Comparison of plunging displacement and $M_\infty = 0.85$ and $V_f = 0.533$.

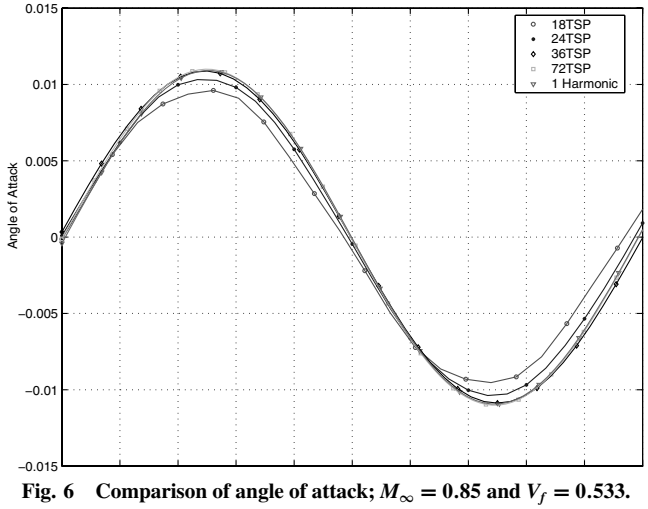

Fig. 6 Comparison of angle of attack; $M_\infty = 0.85$ and $V_f = 0.533$.

Table 1 Comparison of amplitudes and frequencies for various time-accurate and NLFD solutions

Case	$\Delta\alpha$	h/b	ω_f
18 time steps per period	0.0097	0.0182	0.4115
24 time steps per period	0.0104	0.0195	0.4057
36 time steps per period	0.0110	0.0203	0.3972
72 time steps per period	0.0111	0.0206	0.4012
1 harmonic	0.0110	0.0204	0.4045

Figures 7 and 8 illustrate the nondimensional plunge and pitch displacements for various numbers of modes. The simulations were performed at $M_\infty = 0.85$ and $V_f = 0.533$. A close observation reveals that the two- and three-mode cases produced almost identical results, and a slight discrepancy is observed for the one-mode case. However, because the difference is minor, it can be concluded that one mode is again sufficient to acquire aeroelastic solutions for the test cases presented in this work. Note that each period in Figs. 7 and 8 denote the solution after each fluid–structure coupling. At each period, 15 multigrid cycles are computed, and the loads are then transferred to the structural code to update both the plunge and pitch values.

B. Aeroelastic Solutions

The time-accurate aeroelastic solutions were acquired by a forced sinusoidal pitch about the elastic axis at a forcing frequency that is equivalent to w_α. Generally, between one to three periods were computed at the forcing frequency before the airfoil was allowed to displace based on its self-induced loads. The aeroelastic response was computed at various Mach numbers and for a range of speed indices. Typically, three to five cases were computed to gauge the range from stable to unstable responses. At low speed indices, the system damps the forced amplitudes, and both pitch and plunge displacements reach zero displacements. A neutral response occurs at greater speed indices, and as it is increased further, the system becomes unstable and the displacements begin to grow and finally diverge.

In the case of the NLFD approach, both the speed index and the flutter-reduced frequency are modified to reach a neutrally stable solution. The flutter-reduced frequency is then used as the transform frequency for the NLFD approach. The speed index is varied in a manner similar to how the time-accurate runs were performed. In addition, at each speed-index setting, a range of flutter-reduced frequencies is considered. In this work, this range initially centered on the forcing reduced frequency and was modified thereafter. This

Table 2 Time-accurate error in angle-of-attack and plunging displacements using 72 time steps per period as the base solution

	$\|\|h_{\text{error}}\|\|_2$	$\|\|\alpha_{\text{error}}\|\|_2$
18 time steps per period	$3.48e-02$	$1.88e-02$
24 time steps per period	$1.80e-02$	$9.70e-03$
36 time steps per period	$5.00e-03$	$2.70e-03$
1 harmonic	$2.30e-03$	$1.30e-03$

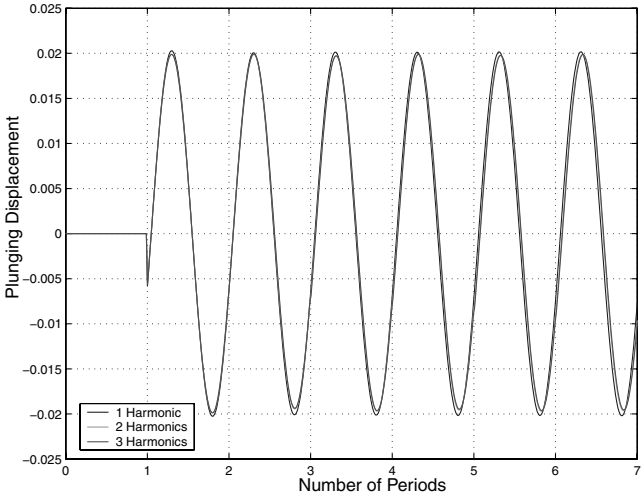

Fig. 7 Nondimensional plunging displacement; $M_\infty = 0.85$ and $V_f = 0.533$.

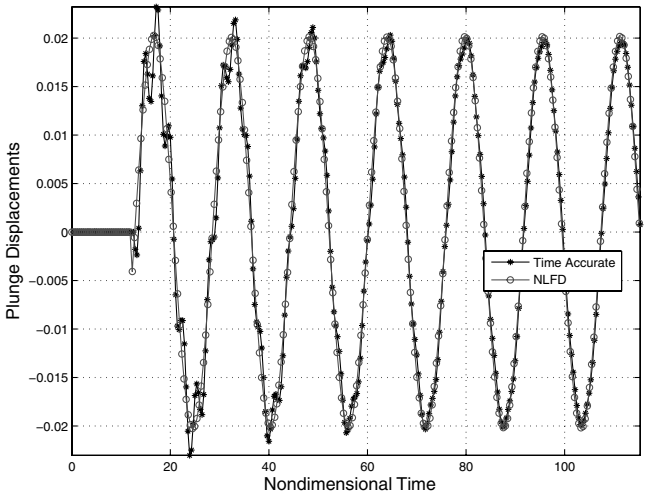

Fig. 9 Neutral response; comparison of plunge displacements; $M_\infty = 0.85$ and $V_f = 0.533$.

certainly increases the computational cost; however, as established later in this subsection, the cost of the NLFD runs are an order of magnitude lower. Therefore, the additional runs due to the change of both the speed index and the flutter-reduced frequency are not prohibitive, but they certainly reduce the overall computational gain of the NLFD approach. Typically, between five to ten additional runs were required to obtain neutral-response solutions for Mach numbers close to the transonic dip and as much as 15 at lower Mach numbers. One possible approach to circumvent this issue, in which the reduced frequency is not known a priori, is to consider a gradient-based algorithm similar to the gradient-based variable time period developed by McMullen [3]. This gradient-based method iteratively determines the time period. The method requires an initial guess of the flutter frequency, and the gradient information is then used to get an updated frequency based on the updated time period after each iteration in the solution process.

Figures 9 and 10 illustrate the full time history of the airfoil neutral response at $M_\infty = 0.85$ for both the time-accurate and NLFD approaches. Both solutions predict final solutions similar to those presented in Figs. 5 and 6; however, there are a couple of important differences: first, the presence of initial transients for the time-accurate solution; second, the discontinuity between the first and second periods in the NLFD solution. In regard to the first difference, engineers are primarily concerned with periodic flow solutions only after they have reached steady state. Unfortunately, when using a time-accurate approach, most of the computational cost is spent resolving the initial decay of transients. Note how these transients persist until the sixth period before the time-accurate code is able to resolve a periodic steady-state solution, as illustrated in Fig. 10. Two additional periods are computed to ensure that a neutral response has been established, requiring a total of eight periods. The NLFD code used to obtain Fig. 10 is able to resolve the same solution in as few as two periods, resulting in a substantial savings. Similar to the time-accurate solutions, several additional periods are calculated to verify that a neutral response has been reached.

The advantages that come with the rapid convergence of the NLFD method are summarized in Table 3. The four factors that contribute to the overall cost are the number of multigrid cycles at each time step, the number of time periods required to reach a periodic steady-state solution, the number of time steps per period, and the additional cost of the Fourier transforms. In this case, 15 multigrid cycles were employed for both solvers to reduce the magnitude of the residual by four orders, as detailed in the previous subsection. Eight periods were required for the time-accurate case, and four periods were required for the NLFD solution to reach a periodic steady-state solution. Both estimates include two additional periods to ensure that a neutral response has been established. As for the number of time steps, the time-accurate calculation used 36 time steps because it provided the least number of time steps to acquire a flutter frequency within three-decimal-place accuracy, as discussed earlier, and three time steps were sufficient for the NLFD solution. And the added cost of the Fourier transforms amounts to 2% for a three-time-step NLFD case. A product of the number of multigrid cycles per time step, the number of time periods and the time steps per period provide for the total number of multigrid cycles required to compute a neutral response. For this test case, the time-accurate

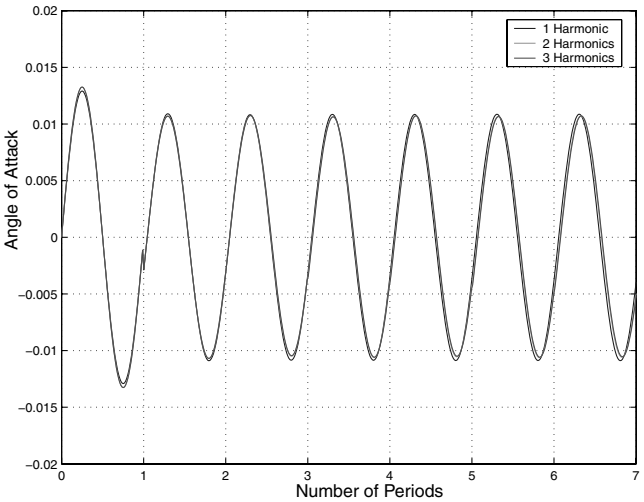

Fig. 8 Angle of attack; $M_\infty = 0.85$ and $V_f = 0.533$.

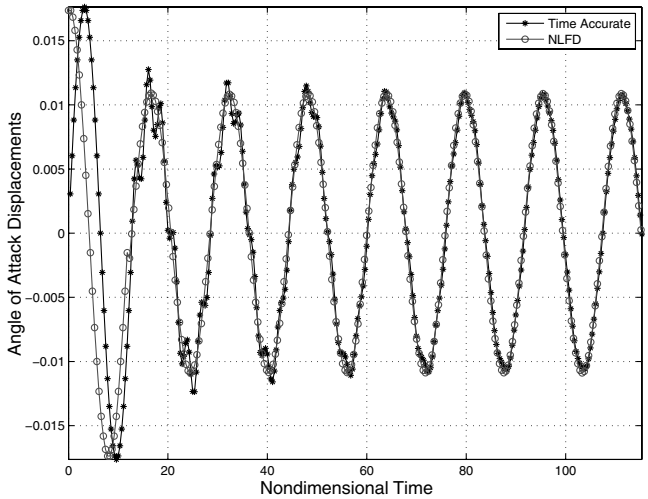

Fig. 10 Neutral response; comparison of angle-of-attack displacements; $M_\infty = 0.85$ and $V_f = 0.533$.

Table 3 Cost comparison between sufficiently accurate NLFD (1 harmonic) and time-accurate (36 time steps per period) methods for flutter analysis

Method	Multigrid cycles	Time periods	Time steps per period	Cost of FFT per multigrid cycle	Overall cost
Time-accurate	15	8	36	1	4320
NLFD	15	4	3	1.02	184

solution required a total of 4320 multigrid cycles, in comparison with the NLFD approach that used 184. A 1.02 factor takes into account the added cost of the Fourier transforms. The final CPU run times for these cases were 19 s for the NLFD and 700 for the time-accurate approach. The number of periods and time steps per period needed to reach a periodic steady-state solution may vary from case to case. However, it remains clear that the NLFD method offers tremendous savings, due to the reduced number of time steps per period needed to resolve the periodic steady-state solution.

The second important distinction between the time-accurate and NLFD results, as mentioned earlier (again, refer to Figs. 9 and 10, for simplicity), is the discontinuity between the first and second periods in the NLFD solution. It is important for the reader to understand that we are solving for the periodic steady-state solution immediately in the NLFD case, bypassing all the transients present in the time-accurate solution. At steady state, the unsteady motion of the airfoil prescribes nonzero loads at zero angle of attack, which, when input in the structural equations, would yield nonzero displacements. So in Fig. 10, periods 2–8 are exactly the same. Essentially, we could have stopped the simulation after the fourth period, because the periodic steady-state solution and a neutral response had already been reached. Even though eight periods are plotted here (done for esthetic reasons and ease of comparison), computing costs and overall run time presented in Table 3 are based on four periods. Because the majority of the cost reduction for the NLFD approach is due to the reduced number of time steps per period needed to resolve the flowfield, the additional periods do not significantly increase the overall cost. Figures 11–14 provide a detailed comparison between time-accurate and NLFD solutions for both damped and diverging solutions at $M_\infty = 0.85$.

The lift- and moment-coefficient histories at Mach 0.85 for both approaches are compared in Figs. 15 and 16. As expected, the time-accurate solution proceeds through a phase of transient solutions before a periodic steady-state solution is demonstrated, compared with the NLFD approach. Figures 17 and 18 show a strong agreement between both the NLFD and time-accurate methods to accurately predict the pressure distribution in the transonic regime at flutter. At this stage of the phase, the airfoil is both moving upward and rotating

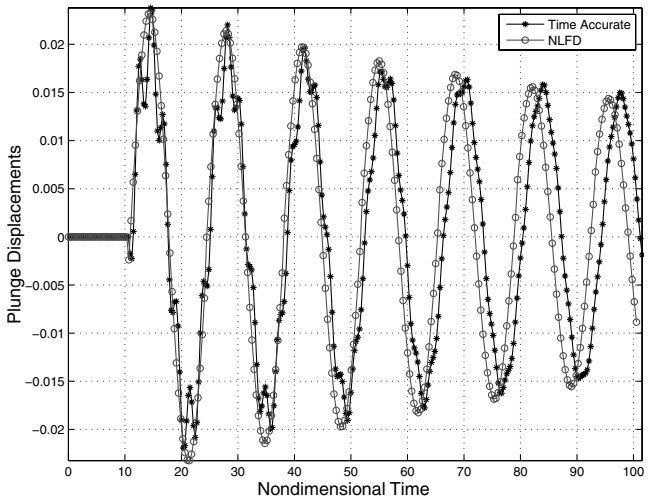

Fig. 11 Damped response; comparison of plunge displacements; $M_\infty = 0.85$ and $V_f = 0.45$.

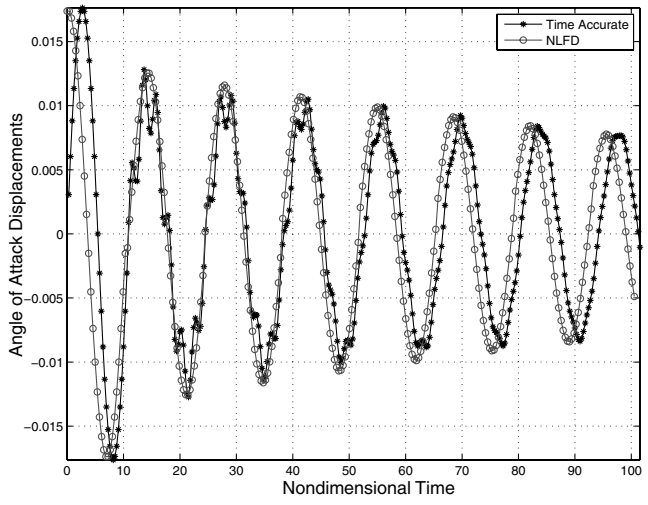

Fig. 12 Damped response; comparison of angle-of-attack displacements; $M_\infty = 0.85$ and $V_f = 0.45$.

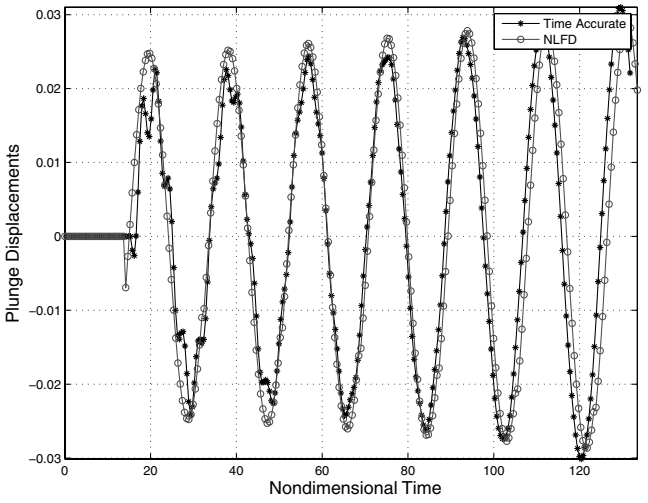

Fig. 13 Diverging response; comparison of plunge displacements; $M_\infty = 0.85$ and $V_f = 0.65$.

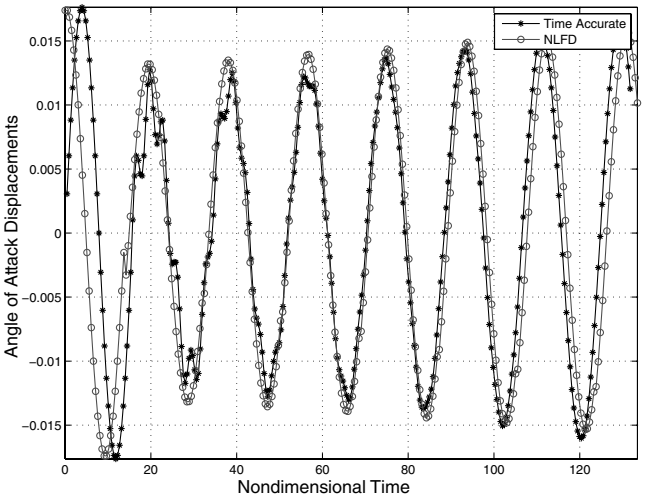

Fig. 14 Diverging response; comparison of angle-of-attack displacements; $M_\infty = 0.85$ and $V_f = 0.65$.

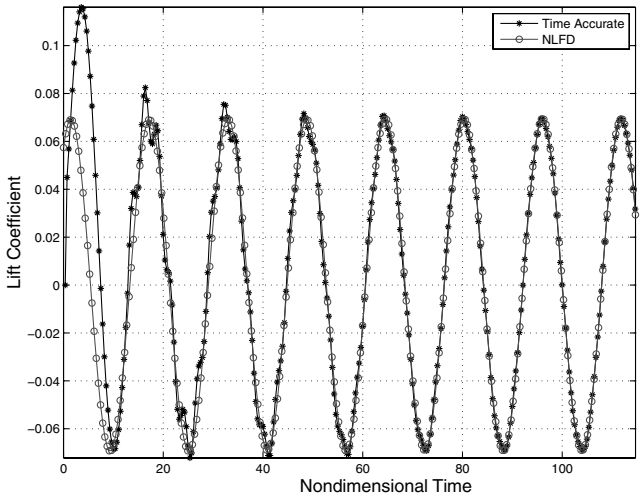

Fig. 15 Convergence of lift coefficient for a neutral response; $M_\infty = 0.85$ and $V_f = 0.533$.

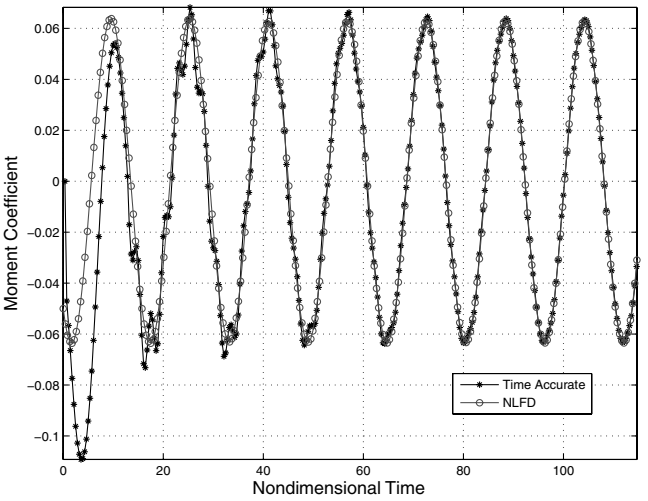

Fig. 16 Convergence of moment coefficient for a neutral response; $M_\infty = 0.85$ and $V_f = 0.533$.

in the clockwise direction, which produces a nonzero pressure difference between the upper and lower surfaces. This implies that a nonzero lift exists and the structural equations would produce nonzero displacements. This provides further assurance as to why we would expect a discontinuity between our forced and steady-state free oscillations (as can be seen between the first and second periods of our NLFD plots).

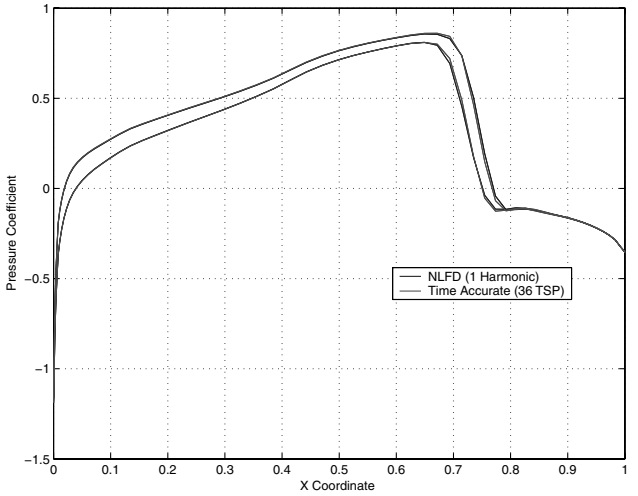

Fig. 17 Pressure distribution at flutter at zero angle of attack; $M_\infty = 0.85$ and $V_f = 0.533$.

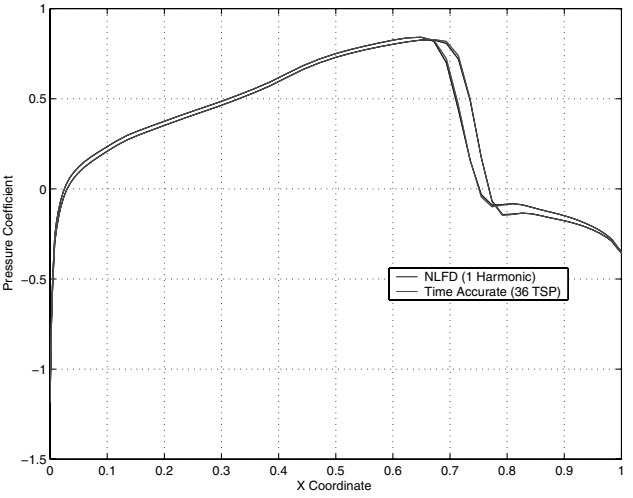

Fig. 18 Pressure distribution at flutter at maximum angle of attack; $M_\infty = 0.85$ and $V_f = 0.533$.

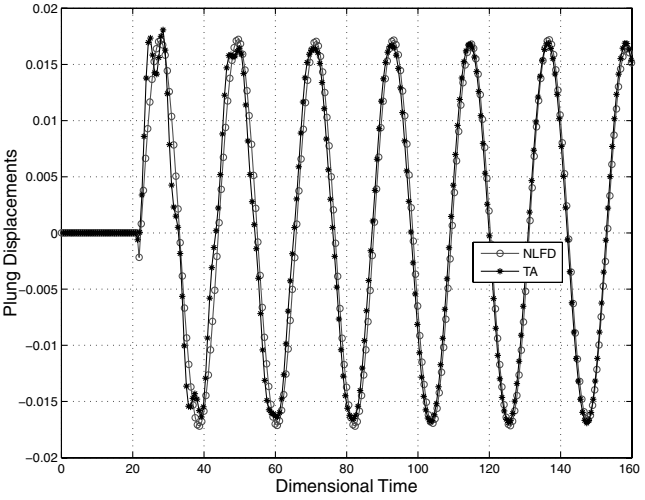

Fig. 19 Neutral-response comparison of plunge displacements (TA=time accurate); $M_\infty = 0.80$ and $V_f = 0.83$.

Figure 19 compares the plunge displacements for a neutral response at Mach 0.85. Table 4 details the plunge, pitch, and flutter frequency for the time-accurate solution with 36 time steps per period and one-mode NLFD solution at the same freestream Mach number. Both solutions produce similar plunge and pitch values within four decimals, and the flutter frequency is within three decimal places.

Finally, a flutter-boundary curve is computed and compared with other existing numerical solutions. A flutter-boundary curve comparing the time-accurate and NLFD methods are presented in Fig. 20. As expected, our transonic dip occurs at $M_\infty = 0.85$ and $V_f = 0.533$ for both the time-accurate and NLFD codes. Our results are in particularly strong agreement with those provided by Alonso and Jameson [4], who used a similar type of flow solver in their aeroelastic computations.

Table 4 Comparison of amplitudes and frequencies for time-accurate and NLFD solutions at Mach 0.80

Case	$\Delta\alpha$	h/b	ω_f
36 time steps per period	0.0102	0.0170	0.2868
1 mode	0.0102	0.0171	0.2891

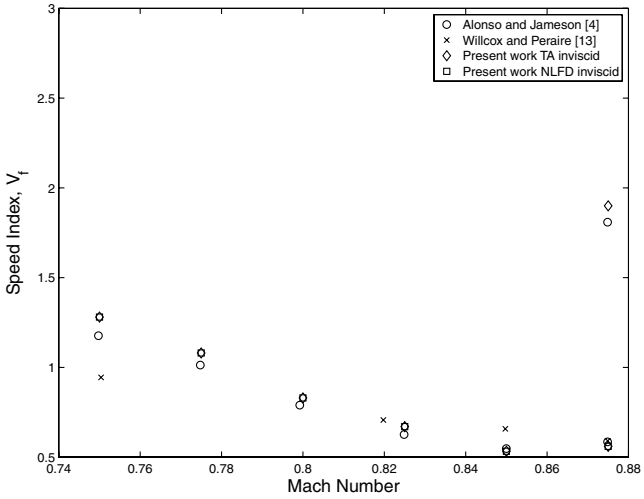

Fig. 20 Flutter-boundary comparison (TA=time accurate).

V. Conclusions

The NLFD method was used to demonstrate aeroelastic solutions in transonic flow. The approach can produce inviscid results that are almost identical to the time-accurate formulation at a fraction of the cost for the test cases performed in this work. A three-time-step NLFD inviscid aeroelastic solution provides for a level of accuracy similar to that produced by the time-accurate approach with 36 time steps per period. Stable, neutral, and unstable responses were demonstrated with just one mode above the zeroth mode. The need to vary the flutter-reduced frequency in addition to the speed index reduces the computational gain of the NLFD approach. Our future work will include the implementation of the gradient-based variable-time-period algorithm to determine the flutter frequency iteratively, and an extension to demonstrate the approach for three-dimensional flows will follow.

Acknowledgments

This research has benefited greatly from the generous support of the Natural Sciences and Engineering Research Council of Canada under Discovery Grant number 206260.

References

[1] Adamczyk, J. J., "Model Equation for Simulating Flows in Multistage Turbomachinery," NASA TM 86869, Nov. 1984.

[2] Hall, K. C., Thomas, J. P., and Clark, W. S., "Computation of Unsteady Nonlinear Flows in Cascades Using a Harmonic Balance Technique," *AIAA Journal*, Vol. 40, No. 5, 2002, pp. 879–886.

[3] McMullen, M., "The Application of Non-Linear Frequency Domain Methods to the Euler and Navier–Stokes Equations," Ph.D. Dissertation, Dept. of Aeronautics and Astronautics, Stanford Univ., Stanford, CA, Mar. 2003.

[4] Alonso, J. J., and Jameson, A., "Fully Implicit Time-Marching Aeroelastic Solutions," AIAA 32nd Aerospace Sciences Meeting and Exhibit, Reno, NV, AIAA Paper 94-0056, Jan. 1994.

[5] Mykytow, W. J., "A Brief Overview of Transonic Flutter Problems," *Unsteady Airloads in Separated and Transonic Flow*, AGARD CP-226, AGARD, Neuilly sur Seine, France, Apr. 1977.

[6] Ashley, H., "Role of Shocks in the 'Sub-Transonic' Flutter Phenomenon," *Journal of Aircraft*, Vol. 17, Mar. 1980, pp. 187–197.

[7] Farmer, M. G., and Hanson, P. W., "Comparison of Supercritical and Conventional Wing Flutter Characteristics," 17th AIAA/ASME/SAE Structures, Structural Dynamics, and Materials Conference, AIAA Paper 1976-1560, Apr. 1976.

[8] Bendiksen, O. O., and Kousen, K. A., "Transonic Flutter Analysis Using the Euler Equations," AIAA Dynamics Specialists Conference, Monterey, CA, AIAA Paper 87-0911, Apr. 1987.

[9] Guruswamy, G. P., "Unsteady Aerodynamic and Aeroelastic Calculations for Wings Using Euler Equations," *AIAA Journal*, Vol. 28, No. 3, Mar. 1990.

[10] Guruswamy, G. P., "Vortical Flow Computations on Swept Flexible Wings Using Navier–Stokes Equations," *AIAA Journal*, Vol. 28, No. 12, Dec. 1990.

[11] Robinson, B. A., Batina, J. T., and Yang, H. T. Y., "Aeroelastic Analysis of Wings Using the Euler Equations with a Deforming Mesh," *Journal of Aircraft*, Vol. 28, No. 6, 1991, pp. 778–788.

[12] Rausch, R. D., Batina, J. T., and Yang, H. T., "Three-Dimensional Time-Marching Aeroelastic Analyses Using and Unstructured-Grid Euler Method," *AIAA Journal*, Vol. 31, No. 9, Sept. 1993, pp. 1626–1633.

[13] Willcox, K., and Peraire, J., "Aeroelastic Computations in the Time Domain Using Unstructured Meshes," *International Journal for Numerical Methods in Engineering*, Vol. 40, No. 13, July 1997, pp. 2413–2431. doi:10.1002/(SICI)1097-0207(19970715)40:13<2413::AID-NME170>3.0.CO;2-E

[14] Blades, E. L., Ruth, M., and Fuhrmann, H. D., "Aeroelastic Analysis of the x-34 Launch Vehicle," 40th AIAA/ASME/ASCE/AHS/ASC Structures, Structural Dynamics and Materials Conference, St. Louis, MO, AIAA Paper 99-1352, 1999.

[15] Farhat, C., Lesoinne, M., and Koobus, B., "A High Fidelity and High Performance Computational Methodology for the Solution of Transient Nonlinear Viscous Aeroelastic Problems," *Proceedings of the First AFOSR Conference on Dynamic Motion CFD*, U.S. Air Force Office of Scientific Research, Wright–Patterson AFB, OH, June 1996, pp. 161–187.

[16] Farhat, C., Lesoinne, M., and Maman, N., "Mixed Explicit/Implicit Time Integration of Coupled Aeroelastic Problems: Three-Field Formulation, Geometric Conservation, and Distributed Solution," *International Journal for Numerical Methods in Fluids*, Vol. 21, No. 10, Nov. 1995, pp. 807–835. doi:10.1002/fld.1650211004

[17] Potsdam, M. A., and Guruswamy, G. P., "A Parallel Multiblock Mesh Movement Scheme for Complex Aeroelastic Applications," AIAA Paper 2001-0716, 2001.

[18] Bendiksen, O., "Modern Developments in Computational Aeroelasticity," *Proceedings of the Institution of Mechanical Engineers, Part G: Journal of Aerospace Engineering*, Vol. 218, No. 3, 2004, pp. 157–177.

[19] Schuster, D. M., Liu, D. D., and Huttsell, L. J., "Computational Aeroelasticity: Success, Progress, Challenge," *Journal of Aircraft*, Vol. 40, No. 5, 2002, pp. 843–856.

[20] Bennett, R. M., and Edwards, J. W., "An Overview of Recent Developments in Computational Aeroelasticity," 29th AIAA Fluid Dynamics Conference, Albuquerque, NM, AIAA Paper 98-2421, June 1998.

[21] Isogai, K., "On the Transonic-Dip Mechanism of Flutter of a Sweptback Wing," *AIAA Journal*, Vol. 17, No. 7, July 1979, pp. 793–795.

[22] Jameson, A., Schmidt, W., and Turkel, E., "Numerical Solutions of the Euler Equations by Finite Volume Methods with Runge-Kutta Time Stepping Schemes," AIAA Paper 81-1259, Jan. 1981.

[23] Jeltsch, R., "Stability on the Imaginary Axis and a Stability of Linear Multistep Methods," *BIT*, Vol. 18, No. 2, 1978, pp. 170–174. doi:10.1007/BF01931693

[24] Gear, C. W., "Numerical Initial Value Problems," Prentice–Hall, Englewood Cliffs, NJ, 1971.

[25] Melson, N. D., Sanetrik, M. D., and Atkins, H. L., "Time-Accurate Navier–Stokes Calculations with Multigrid Acceleration," *Sixth Copper Mountain Conference on Multigrid Methods*, NASA CP-3224, NASA, 1993, pp. 423–437.

[26] Nadarajah, S., and Jameson, A., "Optimal Control of Unsteady Flows Using A Time-Accurate Method," 9th AIAA/ISSMO Symposium on Multidisciplinary Analysis and Optimization Conference, Atlanta, GA, AIAA Paper 2002-5436, Sept. 2002.

[27] Nadarajah, S., McMullen, M., and Jameson, A., "Optimum Shape Design for Unsteady Flows Using Time-Accurate and Nonlinear Frequency Domain Methods," 16th Computational Fluid Dynamics Conference, Orlando, FL, AIAA Paper 2003-3875, June 2003.

[28] Nadarajah, S., and Jameson, A., "Optimum Shape Design for Unsteady Flows with a Time-Accurate Continuous and Discrete Adjoint Method," *AIAA Journal*, Vol. 45, No. 7, 2007, pp. 1478–1491. doi:10.2514/1.24332

[29] Nadarajah, S., and Jameson, A., "Optimum Shape Design for Unsteady Three-Dimensional Viscous Flows Using a Nonlinear Frequency Domain Method," *Journal of Aircraft*, Vol. 44, No. 5, 2007, pp. 1513–1527.

J. Cooper
Associate Editor